Research Square

Preprints are preliminary reports that have not undergone peer review.
They should not be considered conclusive, used to inform clinical practice,
or referenced by the media as validated information.

Thermal Modeling and 3D Geometry Prediction of Multi-layer, Multi-Track Directed Energy Deposition

Sudharshanan Dhabaseelan Vasugi
Stevens Institute of Technology
Chaitanya Krishna Prasad Vallabh
Stevens Institute of Technology
Souran Manoochehri
smanooch@stevens.edu

Stevens Institute of Technology

Research Article

Keywords: Additive manufacturing (AM), Laser powder directed energy deposition (LP-DED), Analytical thermal model, Part geometry prediction

Posted Date: November 16th, 2026

DOI: https://doi.org/10.21203/rs.3.rs-11568989/v1

License: This work is licensed under a Creative Commons Attribution 4.0 International License.
Read Full License

Thermal Modeling and 3D Geometry Prediction of Multi-layer, Multi-Track Directed Energy Deposition

Sudharshanan Dhabaseelan Vasugi, Chaitanya Krishna Prasad Vallabh, Souran Manoochehri*

Department of Mechanical Engineering, Stevens Institute of Technology, Hoboken, NJ 07030, USA

*Corresponding author: Souran Manoochehri, smanooch@stevens.edu

Abstract

Laser powder directed energy deposition (LP-DED) is highly sensitive to process-induced thermal variation, which governs deposition accuracy, surface quality, and solidification microstructure. Analytical thermal models predict meltpool behavior quickly, but multi-layer builds require capturing heat accumulation in an increasingly preheated, geometrically evolving part. This study extends the classical Gaussian moving-source model to multi-layer, multi-track LP-DED of SS316L by incorporating surface heat loss, the enthalpy sink of the powder stream, beam attenuation through the powder cloud, and a spatially resolved layer-to-layer thermal carry-over field. The meltpool width from the predicted isotherms feeds a parabolic bead-geometry model based on powder mass conservation to predict the three-dimensional print profile. Four model parameters are calibrated from a single build using infrared-measured meltpool core temperatures, and the predictions are validated against SS316L thin-walls and cubes. For the thin-walls, the predicted meltpool width and length deviated from measurements by 16.1% and 15.6% on average, and by less than 2% at the lowest scan speed and powder feed rate. For the cubes, the predicted length, width, and height deviated by 13.7%, 8.6%, and 23.1% on average. The deviations of the predictions from the experimental results were investigated and are attributed mainly to treating the attenuated laser energy as entirely lost, which leads to under-predicted meltpool dimensions. This under-prediction can be overcome by properly calibrating the model around the nominal processing window. By rapidly predicting thermal behavior and part geometry, the model offers an efficient basis for process planning, parameter selection, and digital twins.

Keywords: Additive manufacturing (AM) · Laser powder directed energy deposition (LP-DED) · Analytical thermal model · Part geometry prediction

1 Introduction

Laser powder directed energy deposition (LP-DED) has evolved from a cladding and coating technique into a versatile process for fabricating, repairing, and remanufacturing high-value metallic components. Its ability to add material locally, to process a wide range of alloys, and to grade composition within a build has drawn sustained interest from the aerospace, energy, tooling, and biomedical sectors [1, 2]. The same characteristics that make the process flexible also make it difficult to control. Laser–powder–substrate interaction, heat conduction, meltpool convection, rapid solidification, and repeated thermal cycling are tightly coupled over builds that span multiple layers and minutes to hours of deposition, and the resulting thermal cycles produce variations in microstructure and properties along the build height [2, 3].

In LP-DED, metal powder is delivered onto the surface of the substrate, where a moving laser beam melts the powder and forms a meltpool. As the laser advances, the meltpool solidifies into a deposited track, whose cross-section is characterized by its width and height, referred to as the bead width and bead height. A part is built by depositing such tracks side by side, with an overlap, to form a layer, and by stacking successive layers on top of one another. Because each track is deposited onto a substrate or previously deposited material that still carries residual heat from prior tracks, the temperature field, meltpool geometry, and resulting dimensional accuracy are strongly path- and history-dependent. Even minor variations in laser power, scan speed, powder feed rate, hatch spacing, and scanning strategy could therefore produce significant differences in bead height, bead width, and overlap, and ultimately lead to geometric or microstructural defects. Achieving predictable geometry and properties therefore requires an understanding of how the thermal state of the part evolves as it is built, rather than a parameter set selected once and held constant.

In-situ process monitoring captures a large amount of information about the printing process, including thermal, visual, and acoustic signals, each of which carries complementary but distinct information about the same underlying physical events. Coaxial cameras, pyrometers, and infrared cameras have been widely used to track meltpool size and temperature during deposition [4], and such measurements show directly that the thermal state of a multi-layer build does not remain constant. In coaxial monitoring of AISI 316L thin-walls, for example, the meltpool area grew markedly over the build when successive passes were deposited back-to-back, and this growth was

reduced by inter-pass dwell and was smallest for a one-way strategy with a longer dwell [5]. This sensitivity has motivated closed-loop strategies that regulate meltpool temperature through laser power; however, holding the meltpool temperature constant was found not to guarantee uniform track morphology, which led to layer-to-layer adjustment of the laser power profile to address both temperature and morphology [6, 7]. Sensors therefore report what is happening at the meltpool, but they do not by themselves explain how heat inherited from earlier layers and tracks produces it, nor do they predict the deposited geometry before a part is printed. A fast physical model that links the thermal history to meltpool size and bead geometry can complement in-situ sensing, both as a means of interpreting measurements and as a source of process information across a wide parameter space without additional experiments.

Numerical simulation offers a more general route to the thermal history of LP-DED, and finite-element (FE) and thermo-mechanical models have been widely developed to predict temperature histories, meltpool dimensions, residual stress, and distortion [3]. Heigel et al. [8] developed and validated a thermo-mechanical FE model of DED of Ti-6Al-4V, and Wang and Felicelli [9] analyzed the thermal phenomena of LENS deposition numerically. Fetni et al. [10] built a multi-layer FE thermal model of DED of tungsten-carbide-reinforced 316L stainless steel, noting that most modeling studies have focused on single- or few-layer geometries. Such models, however, must resolve a sub-millimeter moving heat source over a part that is centimeters in size and consists of many layers, and their computational demands make them impractical for parameter sweeps, model calibration, or use inside a monitoring or control loop. This cost factor is one of the primary reasons that closed-form and semi-analytical thermal models remain attractive.

Rosenthal's classical moving point-source solution [11] provided the first closed-form description of the quasi-steady temperature field around a traveling heat source on a semi-infinite body, but its point-source idealization overestimates peak temperatures and cannot capture the finite size of a real beam or arc. To address this, Eagar and Tsai [12] introduced a Gaussian-distributed surface heat flux to represent the finite beam radius and energy density distribution of arc and laser sources, which substantially improved the prediction of shallow, wide weld pools. Goldak et al. [13] subsequently proposed the double-ellipsoidal volumetric heat source, allowing independent control of the heat distribution ahead of and behind the source to better match the asymmetric temperature gradients observed in deep-penetration welds. Nguyen et al. [14] later derived closed-

form analytical solutions for these double-ellipsoidal and semi-ellipsoidal moving sources, making such models more tractable for engineering use without resorting to full numerical simulation. Carslaw and Jaeger's treatment of heat in solids [15] remains the mathematical basis for most of these derivations, particularly the use of Green's functions and the method of images to satisfy the adiabatic boundary condition at the top surface of a semi-infinite domain.

Within LP-DED specifically, the above-mentioned welding-derived heat source formulations have been adapted to the powder-fed process, notably by Hu and Kovacevic [16] and, more recently, by Ansari et al. [17], whose analytical single-track model was later extended to single-layer, multi-track deposition through linear superposition of individual track contributions [18]. These contributions established that an analytical Gaussian-source model can predict track-level temperature and geometry with reasonable fidelity at a fraction of the computational cost of full finite-element thermal simulation, making it attractive as a fast, physics-consistent source of process information for monitoring and control applications. Despite these advances, the analytical LP-DED models above were developed mainly for single-track or single-layer deposition, whereas in multi-layer builds residual heat from prior layers measurably shifts meltpool temperature and bead geometry in later layers. Models that extend to multi-layer builds do so by carrying the thermal state of earlier layers into later ones. Mirkoohi et al. [19] used the final temperature of each layer as the initial temperature of the next in an analytical model of laser-based metal additive manufacturing that includes latent heat and temperature-dependent material properties, and Huang et al. [20] added an accumulated temperature field, computed by superposing the transient solutions of prior tracks and layers, to the initial temperature of subsequent layers and tracks.

Reproducing the meltpool of a powder-fed process with a Gaussian conduction solution also requires physics that welding-derived formulations do not include. The powder stream removes energy from the meltpool, since the caught powder must be heated and melted before it contributes to the deposit, and the beam is partially attenuated by the powder cloud before reaching the surface; Pinkerton and Li [21] captured these effects through energy and mass balances, and later work quantified the attenuation with a Beer–Lambert formulation, showing that smaller particles and higher mass flow rates increase the energy loss [22]. Convective transport within the meltpool and surface heat loss over the long timescale of a multi-layer build must likewise be represented for the predicted temperature baseline to remain physical from layer to layer. The deposited geometry,

in turn, is commonly predicted with dedicated geometric models that describe each bead cross-section by an analytical profile such as a parabola and determine how neighboring tracks overlap [23, 24]. Ansari et al. [17, 18] paired such geometry predictions with thermal models for single and multiple tracks, Huang et al. [20] extended a physics-based model to multi-track, multi-layer deposition, and Gockel et al. [25] derived a closed-form solution for the effect of free edges on meltpool geometry in thin-wall builds. Linking temperature to geometry therefore requires two ingredients: the meltpool size, which follows from the temperature field, and the amount of powder captured by the meltpool, from which bead height follows through mass conservation [21]. In multi-track, multi-layer builds, the overlap between tracks and the stacking of layers then determine the final part profile [23, 24].

Building on these principles, our objective in this work is to predict meltpool dimensions and part geometry directly from the process parameters and toolpath. To achieve this, we develop an analytical thermal model for multi-layer, multi-track LP-DED that explicitly accounts for thermal inheritance between layers, together with a parabolic cross-section geometry model that takes the resulting meltpool width to predict multi-layer bead overlap and the complete 3D print profile. The model is calibrated against meltpool measurements from a multi-layer build and then validated on two sets of experimentally printed samples: thin-walls, for meltpool width and length, and cubes, for part dimensions.

2 Methodology overview

The thermal history of a multi-track, multi-layer LP-DED build governs the meltpool size and the geometry of the deposited part, yet it cannot be measured throughout the part during printing and simulating it with finite-element models is too computationally demanding for routine process planning. The objective of this study is therefore to predict the meltpool dimensions and part geometry directly from the process parameters and toolpath by simulating the thermal history of the build with a fast analytical model. To achieve this, the framework implements two models: an analytical thermal model that computes the transient temperature field of the build, and a geometric model that converts the predicted meltpool size into the deposited track and part profiles. Both are calibrated and validated against in-situ measurements and post-build scans of SS316L parts printed by powder-fed laser DED.

The thermal model is used to simulate how the heat input from the laser, together with the heat inherited from previously deposited tracks and layers, raises the temperature of the part and determines the meltpool size along the toolpath. To represent a powder-fed, multi-layer build, it extends the classical Gaussian moving-source solution with surface heat loss, the enthalpy sink of the powder stream, beam attenuation through the powder cloud, and a spatially resolved layer-to-layer thermal carry-over field (Section 3). The geometric model then translates this thermal prediction into the shape of the part: the meltpool width obtained from the predicted isotherm is passed to a parabolic cross-section model that, through powder mass conservation and track overlap, predicts the profile of each track and layer and, ultimately, the complete 3D part (Section 4).

Three sets of SS316L samples were printed on an Optomec LENS MTS 500 system (Optomec, St. Paul, MN, USA): a 30-layer block for calibration, and thin-walls and cubes for validation (Section 5). During printing, a coaxial camera acquires the meltpool width and length, and an infrared camera captures the meltpool core temperature; after printing, we obtain the 3D profile of the printed sample using a 3D optical profilometer (Keyence V700 series 3D scanner, Keyence, Illinois, USA).

The four effective model parameters, namely the enhanced thermal diffusivity factor χ, the effective source radius r_{eff}, the effective loss depth d_{eff}, and the saturation catchment efficiency η_0, were calibrated using the infrared-measured meltpool temperatures of the first five layers of the 30-layer block and were then held fixed. The calibrated model was validated by comparing its predicted meltpool width and length with the coaxial measurements of the thin-walls, and its predicted part length, width, and height with the 3D scans of the cubes.

3 Thermal model for temperature field calculation

An analytical model is developed to describe the transient thermal behavior of the LP-DED process, treating the laser as a moving two-dimensional Gaussian surface heat source on a semi-infinite substrate. The setup and derivation are detailed below. To retain a closed-form, computationally efficient solution, the formulation is based on a set of modeling assumptions, each of which is stated where it is introduced.

3.1 Setup and governing equation

Consider a substrate that occupies the half-space $z \leq 0$ as shown in Fig. 1, with the laser moving along the x −axis at scan speed v. Heat enters only through a surface flux at $z = 0$. Material properties such as thermal conductivity k, density ρ, effective specific heat $c_{p,eff}$, and thermal diffusivity $\alpha = \frac{k_{eff}}{\rho c_{p,eff}}$, with the effective thermal conductivity k_{eff} and $c_{p,eff}$ defined in Section 3.6, are constant. The laser power is denoted as P, the absorptivity as A, the beam radius as r_b, and the ambient temperature as T_0. The semi-infinite domain is adopted because it admits a closed-form Green's function solution and represents the substrate on which the part is built; the finite height of the part is accounted for through the layer-wise effective loss depth (Eq. (8)) and the inherited temperature field of each layer.

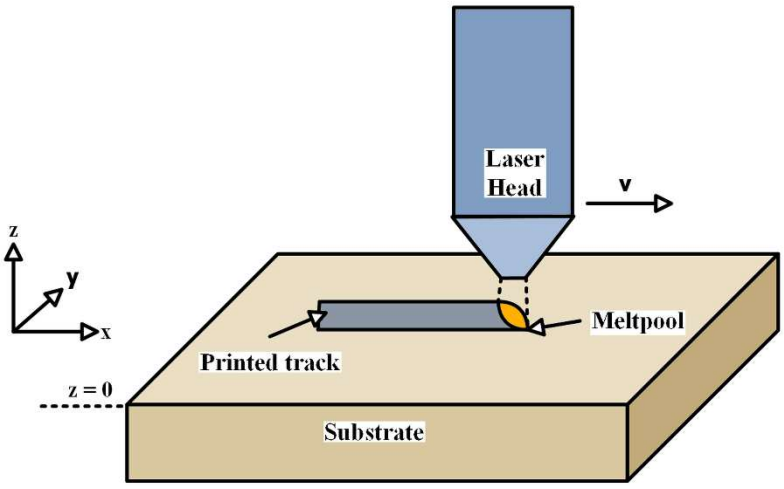


Fig. 1 *Schematic of the coordinate system and moving heat source: the substrate occupies the half-space z ≤ 0, with the laser moving along x at scan speed v and depositing a single track*

The reduced-order mathematical approximation of the governing transient heat conduction equation is given by

$$\rho c_{p,eff} \left(\frac{\partial T}{\partial t}\right) = k\nabla^2 T - \left(\frac{2h_{surf}}{d_{eff}}\right)(T - T_0),\ z < 0 \qquad (1)$$

with Neumann boundary condition $k\left(\frac{\partial T}{\partial z}\right)|_{z=0} = q(x, y, t)$ and initial condition $T(x, y, z, 0) = T_0$.

The term $\left(\frac{2h_{surf}}{d_{eff}}\right)(T - T_0)$ represents the lumped surface heat loss to the environment, with h_{surf} a combined radiative and convective heat-transfer coefficient and d_{eff} an effective loss depth. This term is retained because, over the timescale of a multi-layer build, surface losses are not negligible relative to conduction into the substrate. Neglecting them causes the predicted inter-layer baseline temperature to ramp without bound rather than converging to a plateau, which is inconsistent with the physics.

For a track n centered at y_n starting at time t_n , the Gaussian surface flux is given by

$$q_n(x, y, t) = \left(\frac{2P_{abs}}{\pi r_b^2}\right) \cdot exp\left[-\frac{2\left(\left(x - v(t - t_n)\right)^2 + (y - y_n)^2\right)}{r_b^2}\right] \cdot H(t - t_n) \quad (2)$$

where $H(\cdot)$ is the Heaviside step function, which turns the flux for track n on at its start time t_n and the factor $\frac{2P_{abs}}{\pi r_b^2}$ is chosen so that integrating the flux over the entire surface recovers the total absorbed laser power, $\iint q_n \, dx \, dy = P_{abs}$, where P_{abs} is the laser power absorbed after attenuation through the powder cloud, defined in Eq. (13).

3.2 Closed-form temperature solution for single-track prints

The temperature rise $\Delta T = T - T_0$ produced by the surface flux is obtained by convolving that flux with the Neumann Green's function for a semi-infinite solid, where G, evaluated at the source plane $z' = 0$, is:

$$G|_{z'=0} = \left[\frac{2}{(4\pi\alpha\tau)^{\frac{3}{2}}}\right] \cdot exp\left[\frac{-((x - x')^2 + (y - y')^2 + z^2)}{4\alpha\tau}\right] \quad (3)$$

where $\tau = t - t'$, and (x', y', z') and t' denote the position and time of the source. The temperature rise for a single track $(t_n = 0, y_n = 0)$ is given by

$$\Delta T(x, y, z, t) = \left(\frac{1}{\rho c_{p,eff}}\right) \int_0^t \iint G|_{z'=0} \cdot \, q(x', y', t') \, dx' dy' dt' \quad (4)$$

Substituting q and G , the combined spatial integral evaluates in closed form to:

$$I(x,y,\tau) = \left[\frac{4\pi\alpha\tau\, r_b^2}{(r_b^2 + 8\alpha\tau)}\right] \cdot exp\left[-\frac{2\left(\left(x - v(t-\tau)\right)^2 + y^2\right)}{(r_b^2 + 8\alpha\tau)}\right] \quad (5)$$

where I is the spatial part of the convolution, i.e., the integral over x′ and y′ of the Gaussian factors of q and G, with the amplitude constants and the depth factor $exp\left(-\frac{z^2}{4\alpha\tau}\right)$ kept outside the integral. Substituting Eq. (5) back into the convolution of Eq. (4) collapses the problem to a single remaining time integral, which is evaluated below once the surface-loss term has been incorporated.

3.3 Surface heat loss and single-track solution

The surface-loss term introduced in Eq. (1) is linearized about the mean film temperature. The radiative contribution is

$$h_{rad} = \varepsilon\, \sigma_{SB}\left(T_{film}^2 + T_\infty^2\right)\left(T_{film} + T_\infty\right) \quad (6)$$

where ε is the surface emissivity, σ_{SB} the Stefan–Boltzmann constant, $T_\infty = T_0 + 273$ the ambient temperature in Kelvin, and $T_{film} = ½(T_m + T_0) + 273$ the mean film temperature, with T_m the melting temperature. The total surface coefficient is $h_{surf} = h_{rad} + h_{conv}$, where h_{conv} is the convective heat-transfer coefficient.

Defining a lumped loss rate $b = \frac{2h_{surf}}{\rho\, c_{p,eff}\, d_{eff}}$ and substituting $\theta = (T - T_0)e^{bt}$ reduces the loss-modified equation to the Green's-function form. The transient temperature rise for a single track at $t = 0$, centered at $y = 0$ is given by

$$\Delta T_n(x,y,z,t) = \frac{2P_{abs}}{\left(\rho c_{p,eff}\pi^{\frac{3}{2}}\sqrt{\alpha}\right)} \cdot \int_0^t \frac{1}{\left(\sqrt{\tau}\left(r_{eff}^2 + 8\alpha\tau\right)\right)} \cdot exp\left\{-\frac{z^2}{4\alpha\tau} - \frac{2\left[\left(x - v(t-\tau)\right)^2 + (y)^2\right]}{\left(r_{eff}^2 + 8\alpha\tau\right)} - b\tau\right\} d\tau \quad (7)$$

where P_{abs} is the laser power absorbed after attenuation through the powder cloud, defined in Eq. (13), and r_{eff} an effective source radius, which replaces the beam radius r_b to represent the spatial distribution of the absorbed energy and is one of the four calibrated parameters. Since the effective loss depth increases as the part grows taller, b is re-evaluated for each layer L, with Δz denoting the layer height, as

$$d_{eff}^{L} = d_{eff} + (L - 1)\Delta z \tag{8}$$

3.4 Powder-stream enthalpy sink

Powder delivered into the meltpool absorbs sensible and latent heat before contributing to deposited mass and therefore acts as a distributed heat sink spatially co-located with the pool. The net temperature rise is the superposition of the laser source and this sink, both evaluated with the form of Eq. (7) but at different radii and amplitudes:

$$\Delta T_{net} = \Delta T(r_{eff}, C_L) - \Delta T(r_{ps}, C_S) \tag{9}$$

where r_{ps} is the powder-stream radius, and C_L and C_S are the amplitude constants of the laser source and the powder sink, respectively, obtained from the prefactor of Eq. (7) with P_{abs} and P_{sink} as the source power:

$$C_L = \frac{2P_{abs}}{\rho\, c_{p,eff}\, \pi^{\frac{3}{2}} \alpha^{\frac{1}{2}}}, \quad C_S = \frac{2P_{sink}}{\rho\, c_{p,eff}\, \pi^{\frac{3}{2}} \alpha^{\frac{1}{2}}} \tag{10}$$

The sink power P_{sink} is the rate at which enthalpy is consumed heating and melting the caught powder fraction:

$$P_{sink} = \eta_c\, F \left[\bar{c}_{\mathrm{p}} (T_m - T_0) + L_f \right] \tag{11}$$

with F the powder feed rate in kg s^{-1}, $\bar{c}_{\mathrm{p}}$ the range-averaged specific heat, L_f the latent heat of fusion, and η_c the catchment efficiency of Eq. (22), which in the thermal model is evaluated at a nominal meltpool width estimated from the nominal layer height and the process parameters, so that P_{sink} is constant over the build; the geometry model (Section 4) then evaluates η_c for each

track from its predicted meltpool width. The net power available to raise the part temperature is $P_{net} = P_{abs} - P_{sink}$. The caught powder is assumed to enter the meltpool at ambient temperature, i.e., its in-flight heating by the beam (Section 3.5) is neglected, which increases the powder enthalpy sink.

3.5 Beam attenuation through the powder cloud

The beam is partially obstructed by powder particles crossing it before it reaches the deposition surface. Modeling the beam profile using Beer–Lambert attenuation along the beam–powder interaction length reduces the laser power reaching the deposition surface by the fraction intercepted by the powder cloud. This intercepted power is entirely removed from the meltpool energy balance. In the printing process, part of the intercepted power is absorbed by the particles, and the heated particles that are deposited on the meltpool return this energy back to the meltpool [26]. The power absorbed by the scattered powder that is not deposited on the meltpool is lost in this process. The present model therefore represents an upper bound on the energy loss associated with the powder stream, and hence a smaller estimate of the available energy for melting, compared to the actual LP-DED print process. This observation is consistent with the analysis presented in Frenk et al. [26], which concludes that the used formulation underestimates the measured laser power. Since the attenuation increases with the powder feed rate, the model increasingly overestimates the energy loss as the feed rate increases. This can be resolved through experimental calibration that accounts for the range of the feed rate.

To obtain the optical thickness of the powder cloud (τ_{att}), the Beer–Lambert model [26] is utilized. In this model, the particles are assumed to be spherical with a uniform diameter (d_p) and to be uniformly dispersed over the powder-stream cross-section (πr_{ps}^2). Since d_p is much larger than the laser wavelength, each particle intercepts the beam power incident on its projected area ($\frac{\pi d_p^2}{4}$). The powder mass concentration in the stream is $\frac{F}{\pi r_{ps}^2 v_p}$, and dividing it by the particle mass $\rho_{pw} \frac{\pi d_p^3}{6}$ gives the number of particles per unit volume, so that the optical thickness of the powder cloud and the fraction of the beam power transmitted through it can be obtained by Eq. (12).

$$\tau_{att} = \frac{1.5\, F\, l_{int}}{\left(\rho_{pw}\, v_p\, \pi\, r_{ps}^2\, d_p\right)}, \quad \eta_{att} = exp(-\tau_{att}) \tag{12}$$

where η_{att} is the fraction of the beam power transmitted to the deposition surface, F the powder feed rate, l_{int} the interaction path length, v_p the particle velocity, d_p the mean particle diameter, and ρ_{pw} the density of the powder particle material, equal to ρ (Table 1). The absorbed power (P_{abs}) can be obtained by the following equation

$$P_{abs} = A\, \eta_{att}\, P \tag{13}$$

where A is the absorptivity of the deposition surface, i.e., the fraction of the transmitted beam power absorbed by the surface. This absorbed power can be substituted in Eq. (10) to obtain the amplitude constant C_L. Since τ_{att} is proportional to F, the absorbed power decreases exponentially with powder feed rate, so that, together with the powder enthalpy sink of Eq. (11), a higher feed rate reduces the net energy available for melting and hence the meltpool size.

3.6 Effective properties and the enhanced thermal diffusivity factor

The material properties are averaged over the range from ambient to melting, and the latent heat of fusion is folded into an effective specific heat so that melting is represented without tracking an explicit phase-change front:

$$c_{p,eff} = \bar{c}_{\mathrm{p}} + \frac{L_f}{(T_m - T_0)} \tag{14}$$

To compensate for convective transport within the meltpool, a dimensionless factor χ is introduced:

$$k_{eff} = \chi\, \bar{k}, \quad \alpha = \frac{k_{eff}}{\left(\rho\, c_{p,eff}\right)} \tag{15}$$

The factor χ is calibrated against the measured meltpool temperature. Together with the effective source radius r_{eff} (Section 3.3), the effective loss depth d_{eff} (Eq. (1)), and the saturation catchment efficiency η_0 (Eq. (22), Section 4.1), these constitute the four calibrated parameters of

the model, all of which were calibrated iteratively until the predicted meltpool temperature agreed with the temperature measured by the infrared camera (Section 6). The calibrated parameters are specific to the LP-DED system, powder, and material used in this study; applying the model to a different system or material would require recalibration. All other inputs are measured process settings or tabulated material properties.

3.7 Multi-track superposition

For a single-layer print with N parallel tracks (hatch spacing h_s, track length l_{trk}), each track n is centered at $y_n = (n-1)h_s$ and starts at $t_n = (n-1)(l_{trk} + h_s)/v$, where h_s/v is the time required to step over to the adjacent track, as shown in Fig. 2. For the bidirectional scan pattern used in this study, the scan direction alternates between successive tracks, which is accounted for by reversing the sign of v in Eq. (17) and starting each track at the end of the previous one.

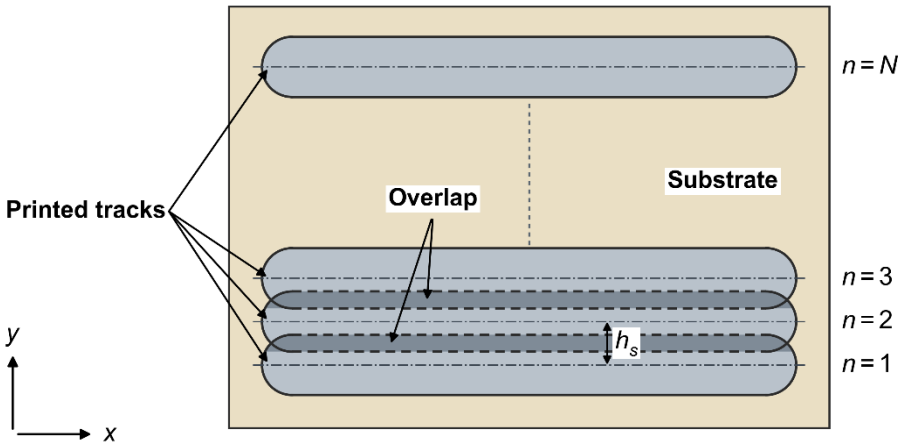


Fig. 2 *Top-down view of multi-track superposition within a single layer*

Since the governing heat equation is linear, the total field is the superposition of individual track contributions:

$$T(x, y, z, t) = T_0 + \Sigma_{n=1}^{N} \Delta T_n(x, y, z, t) \tag{16}$$

$$\Delta T_n(x,y,z,t) = \frac{2P_{abs}}{\left(\rho c_{p,eff}\pi^{\frac{3}{2}}\sqrt{\alpha}\right)} \cdot H(t-t_n)\int_0^{t-t_n} \frac{1}{\left(\sqrt{\tau}\left(r_{eff}^2 + 8\alpha\tau\right)\right)} \cdot exp\left\{-\frac{z^2}{4\alpha\tau} - \frac{2\left[\left(x - v(t-t_n-\tau)\right)^2 + (y-y_n)^2\right]}{\left(r_{eff}^2 + 8\alpha\tau\right)} - b\tau\right\} d\tau \quad (17)$$

In Eq. (16), ΔT_n is the net temperature rise of Eq. (9) for track n, whose laser contribution is given by Eq. (17); the sink contribution takes the same form with r_{ps} and P_{sink} in place of r_{eff} and P_{abs}. The Heaviside factor ensures tracks that have not yet started contributing zero, and each track integrates only over the elapsed time since it began.

3.8 Multi-layer temperature field calculation

The single-track and multi-track formulations discussed assume that deposition starts on a substrate at room temperature. While this assumption is valid for the first layer, it does not hold for the subsequent layers. As each layer is printed, the residual heat from the completed layers raises the temperature of the print part where the next layer will be deposited. Therefore, the initial condition for each layer cannot be treated as constant.

To account for this, the initial condition for each layer is inherited as a spatially resolved temperature field rather than as a single averaged value, since the region beneath the end of a layer's toolpath is hotter than the region beneath its start when the next layer begins, as illustrated in Fig. 3. At the end of each inter-layer dwell, the field carried forward to layer $L + 1$ is

$$T_0^{L+1}(x,y) = G_\sigma\left[T_0 + (T_0^L(x,y) - T_0)e^{-b\,\Delta t_L}\right] + \Delta T_{carry}^L(x,y) \quad (18)$$

where $G_\sigma[\cdot]$ denotes a two-dimensional Gaussian blur of width $\sigma = \sqrt{4\alpha\Delta t_L}$ representing in-plane conduction during the dwell, Δt_L is the layer scan duration plus dwell, and ΔT_{carry}^L is the completed layer's own contribution evaluated at the additional dwell time via Eq. (9). During layer L, the inherited field replaces T_0 in Eq. (16) and decays at the loss rate b, i.e., $T = T_0 + (T_0^L(x,y) - T_0)exp[-b(t - t_{L,0})] + \sum \Delta T_n$, where $t_{L,0}$ is the start time of layer L. As shown

in Eq. (18), the blur is applied only to the inherited field and not to the contribution of the completed layer.

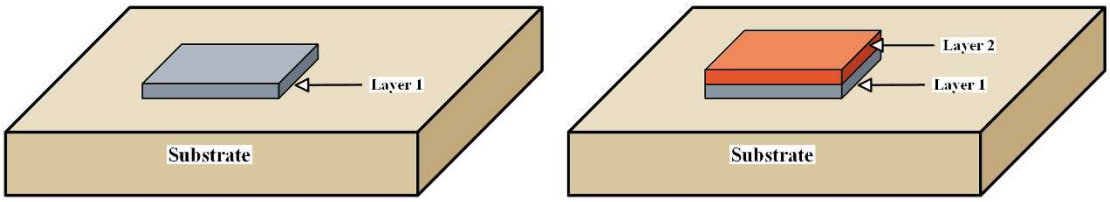


Fig. 3 *Schematic of thermal inheritance between layers: Layer 2 inherits the spatially resolved temperature field $T_0^{(1)}(x, y)$ left by Layer 1, rather than starting from a uniform ambient temperature*

3.9 Model parameters

The material properties of SS316L used in this work are summarized in Table 1.

Table 1 *Material Properties for SS316L*

Property	Symbol	Value
Density	ρ	8000 kg m^{-3}
Thermal conductivity at 25 °C	k_{25}	16 W m^{-1} K^{-1}
Thermal conductivity at T_m	k_{Tm}	30 W m^{-1} K^{-1}
Range-averaged conductivity	$\bar{k}$	23 W m^{-1} K^{-1}
Specific heat at 25 °C	$c_{\mathrm{p},\,25}$	500 J kg^{-1} K^{-1}
Specific heat at T_m	c_{p}, Tm	800 J kg^{-1} K^{-1}
Range-averaged specific heat	$\bar{c}_{\mathrm{p}}$	650 J kg^{-1} K^{-1}
Latent heat of fusion	L_f	2.70 × 10^5 J kg^{-1}
Melting temperature	T_m	1400 °C
Ambient temperature	T_0	25 °C

This extended model was applied to a 20 × 20 × 15 mm, 30-layer SS316L sample, deposited with a bidirectional alternating pattern as shown in Fig. 4, with laser power = 350 W, scan speed = 300 mm/min, powder feed rate = 2 g/min, and hatch spacing = 0.35 mm.

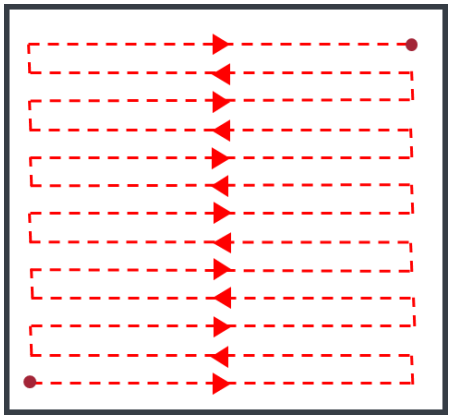


Fig. 4 *Bidirectional scanning pattern for printing a layer*

4 Cross-section profile prediction

With the transient temperature field established, the deposited track geometry can now be predicted, specifically the cross-sectional profile of each track, from which the print height is obtained. The steady-state cross-section of a single deposited track, taken perpendicular to the scan direction, is approximated by a parabolic profile, as the meniscus shape of a locally Gaussian meltpool is closely matched by a second-order polynomial in the transverse coordinate y [23, 24]. Each track i is therefore represented as a parabola:

$$f_i = a_i y^2 + b_i y + c_i \tag{19}$$

with three unknown coefficients determined by three physically motivated conditions: height continuity with the left and right neighboring tracks, and conservation of the deposited cross-sectional mass.

Let A_i and B_i denote the y-coordinates where track i meets its left neighbor j and right neighbor r, located at $A_i = y_i - W_i/2$ and $B_i = y_i + W_i/2$, where y_i is the centerline position of track i and W_i its width (Section 4.1). Height continuity requires:

$$f_i(A_i) = f_j(A_i),\ f_i(B_i) = f_r(B_i) \tag{20}$$

Thus, the bead profile meets its neighbors without a step discontinuity at the overlap boundary. The third condition conserves the cross-sectional area under f_i between A_i and B_i . For a parabolic segment of width W_i and peak height h_i, integrating the parabola over its base gives the standard result that it occupies two-thirds of its bounding rectangle:

$$\int f_i\, dy = \left(\frac{2}{3}\right) W_i\, h_i \tag{21}$$

4.1 Meltpool width extraction and powder catchment

The track width W_i from the T_m isotherm of the temperature field computed in Section 3, evaluated on a local neighborhood centered on the instantaneous laser position, and taken as the transverse extent of the closed isotherm contour that encloses the laser. The meltpool width is thus obtained directly from the predicted temperature field, which links the deposited geometry to the thermal history without additional empirical input.

The peak bead height h_i is extracted from the powder catchment mass balance. The catchment efficiency, defined as the fraction of delivered powder incorporated into the bead, is modeled as saturating with meltpool width, since a wider pool intercepts a larger share of the powder stream:

$$\eta_c(W) = \eta_0 \left[1 - exp\left(-\frac{W^2}{\left(2\, r_{ps}^2\right)}\right)\right] \tag{22}$$

where η_0 is the saturation catchment efficiency, and Eq. (22) corresponds to the fraction of a Gaussian powder stream of radius r_{ps}, defined at 1/e² of its peak flux, that falls within a circular meltpool of diameter W. The deposited cross-sectional area per track follows from conservation of powder mass:

$$A_{dep,i} = \frac{\eta_c(W_i) F}{\left(\rho_{pw}\, v\right)} \tag{23}$$

Combining Eq. (23) with the two-thirds parabolic area identity of Eq. (21) gives the peak bead height:

$$h_i = \frac{3A_{dep,i}}{(2W_i)} \tag{24}$$

4.2 Mass conservation and overlap

The three conditions link the meltpool geometry (W_i, h_i) from the thermal model directly to the deposited cross-sectional area. Accounting for previously deposited material still present under the current bead's footprint, the full mass conservation condition is:

$$\int_{A_i}^{B_i} f_i\,(y)\,dy = \left(\frac{2}{3}\right) W_i\, h_i + \Sigma_{m=1}^{\psi} \int_{l_m}^{l_{m+1}} f_{Q_{n,m}}(y)\,dy \tag{25}$$

where ψ represents the number of prior-track segments overlapping track i, and the summation accounts for residual area from earlier tracks $Q_{n,m}$ (with n the index of the earlier track and m the index of the overlapping subinterval) occupying subintervals $[l_m, l_{m+1}]$ within $[A_i, B_i]$ that are not fully re-melted by track i. Equations (20) and (25) give three equations in the three unknowns (a_i, b_i, c_i), solved sequentially track-by-track to construct the full single-layer overlap profile, as shown in Fig. 5a.

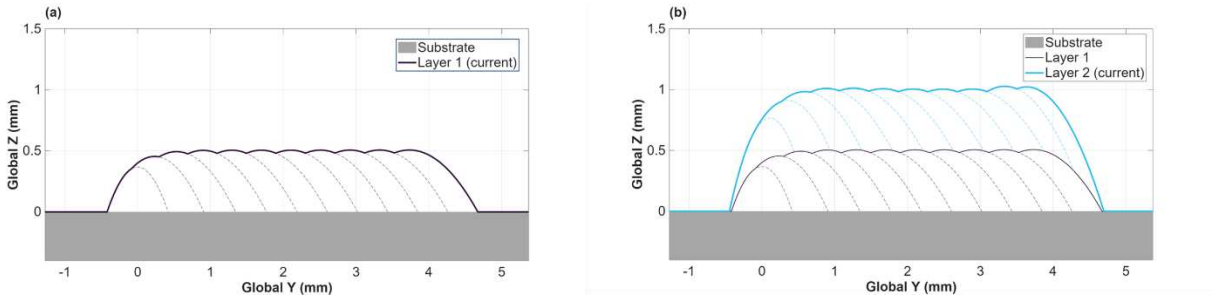


Fig. 5 *Predicted cross-sectional profiles: (a) a single deposited layer, showing the individual overlapping track parabolas (dashed) and the resulting layer surface (solid); (b) two stacked layers, showing how the track parabolas (dashed) of each layer combine into a surface profile that becomes the base for the next layer*

4.3 Multi-layer extension

For multi-layer prints, each new layer L is deposited on the finished surface of layer $L-1$, denoted $g_{L-1}(y)$, rather than a flat baseline. The boundary and mass conservation conditions therefore carry over in the same form, but every height is now measured relative to $g_{L-1}(y)$ instead of a flat baseline of zero; that is, f_i and $f_{Q_{n,m}}$ in Eq. (25) each are replaced by their height above the previous layer's surface, $f_i^{(L)}(y) - g_{L-1}(y)$:

$$\begin{aligned} &\int_{A_i}^{B_i} [f_i^{(L)}(y) - g_{L-1}(y)]\, dy \\ &= \left(\frac{2}{3}\right) W_i\, h_i + \Sigma_{m=1}^{\psi} \int_{l_m}^{l_{m+1}} [f_{Q_{n,m}}^{(L)}(y) - g_{L-1}(y)]\, dy \end{aligned} \tag{26}$$

with W_i, h_i now taken from the multi-layer thermal model at the corresponding track midpoint in the layer L. The meltpool size depends on the layer-wise temperature field, which itself depends on the accumulated geometry of all preceding layers. The algorithm is applied iteratively, layer by layer. After fitting each layer, the track polynomials are combined into a single surface profile $g_L(y)$, which then serves as the base surface for the next layer $L+1$. This ensures later layers correctly inherit the top-surface profile of the layer below, as illustrated in Fig. 5b.

Applying the layer-by-layer procedure of Eq. (26) across every track of every layer yields the complete deposited geometry, since the combined surface profile $g_L(y)$ of each layer is retained and stacked on the one below it. The generated profile reproduces the layer-wise build-up of the part, and the taper toward the free edges, where the outermost tracks are laterally supported on one side only. The lateral extent of the predicted part is thus defined by the meltpool boundary of the outermost tracks, i.e., by the deposited material that is fused by the meltpool.

The thermal and geometric models are implemented in MATLAB R2025b (MathWorks, Natick, MA, USA) with GPU acceleration, and all simulations were performed on a workstation with an AMD Ryzen Threadripper PRO 3955WX processor (16 cores, 3.90 GHz), 192 GB of RAM, and an NVIDIA RTX 6000 Ada Generation GPU (48 GB). The resulting computation times are reported in Section 6.

5 Experimental study

All specimens were fabricated on an Optomec LENS MTS 500 (Optomec, St. Paul, MN, USA) DED machine with a maximum laser power of 500 W. The beam can be set to several spot sizes, but a beam spot diameter of 0.5 mm was used for all builds in this study. Powder was delivered through a coaxial nozzle with four powder jets, using argon as the carrier and shielding gas. Fig. 6a shows the experimental setup, including the laser head, the substrate, the two sensors, and the coordinate system used in the model. The process was monitored with two sensors. A coaxial FLIR Blackfly S camera (Teledyne Vision Solutions, Richmond, BC, Canada), incorporating a Sony IMX273 color CMOS sensor (3.6 × 3.6 mm focal plane, 800 × 800 pixels) without an infrared filter and capable of capturing up to 226 frames per second, viewed the deposition along the beam axis and recorded the meltpool; the meltpool width W and length L were extracted from each frame as illustrated in Fig. 6b. An Optris PI 05M infrared camera (Optris GmbH, Berlin, Germany), operating in the 500–540 nm spectral range, which is suited to the low emissivity of reflective metal surfaces, and covering a temperature range of 950–2450 °C, recorded the temperature field around the meltpool, from which the meltpool core temperature was taken from each frame (Fig. 6c), using an emissivity setting of 0.4.

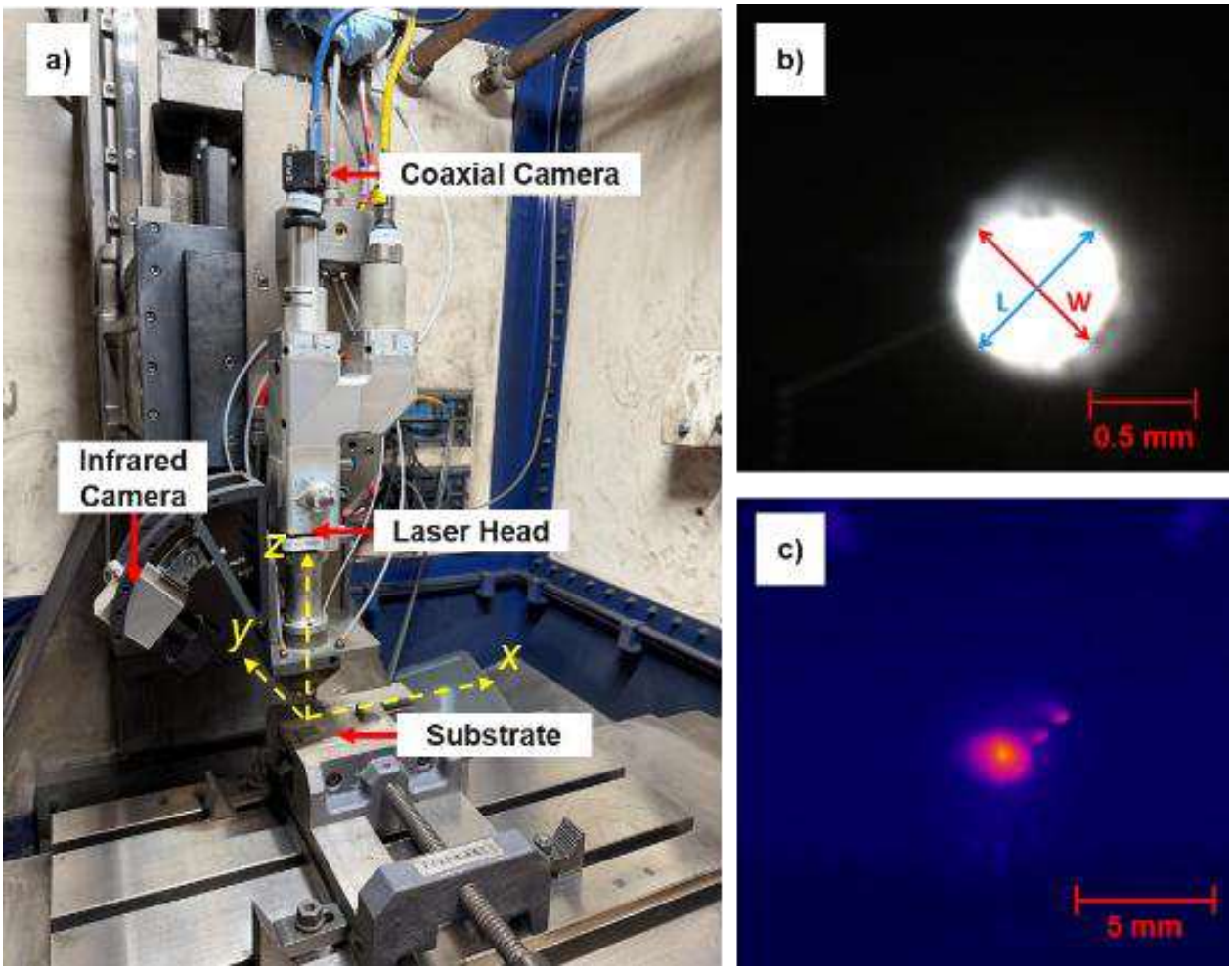


Fig. 6 *Experimental setup: (a) Optomec LENS MTS 500 deposition head with the coaxial camera, the infrared camera, the substrate, and the coordinate system used in the model; (b) coaxial image of the meltpool with the fitted meltpool width W and length L; (c) infrared image showing the meltpool hot spot*

The metal powder used for printing in this study was SS316L stainless steel powder (Carpenter Additive, Widnes, United Kingdom) with a particle size range of 45–106 μm. All parts were deposited on SS316L substrate plates that were sandblasted before deposition and were not preheated. The SS316L properties used in the thermal model are listed in Table 1.

Three sets of SS316L samples were printed for this study: a 20 × 20 × 15 mm, 30-layer block (Fig. 7a), four thin-wall samples (20 mm long with 20 layers; Fig. 7b), and four 5 × 5 × 2.5 mm cubes (5 layers; Fig. 7c). All samples were deposited with a layer height of 0.5 mm. The 30-layer block was used for model calibration, whereas the thin-walls and cubes were used for model validation;

the process parameters of each build, the calibration procedure, and the validation results are presented in Section 6.

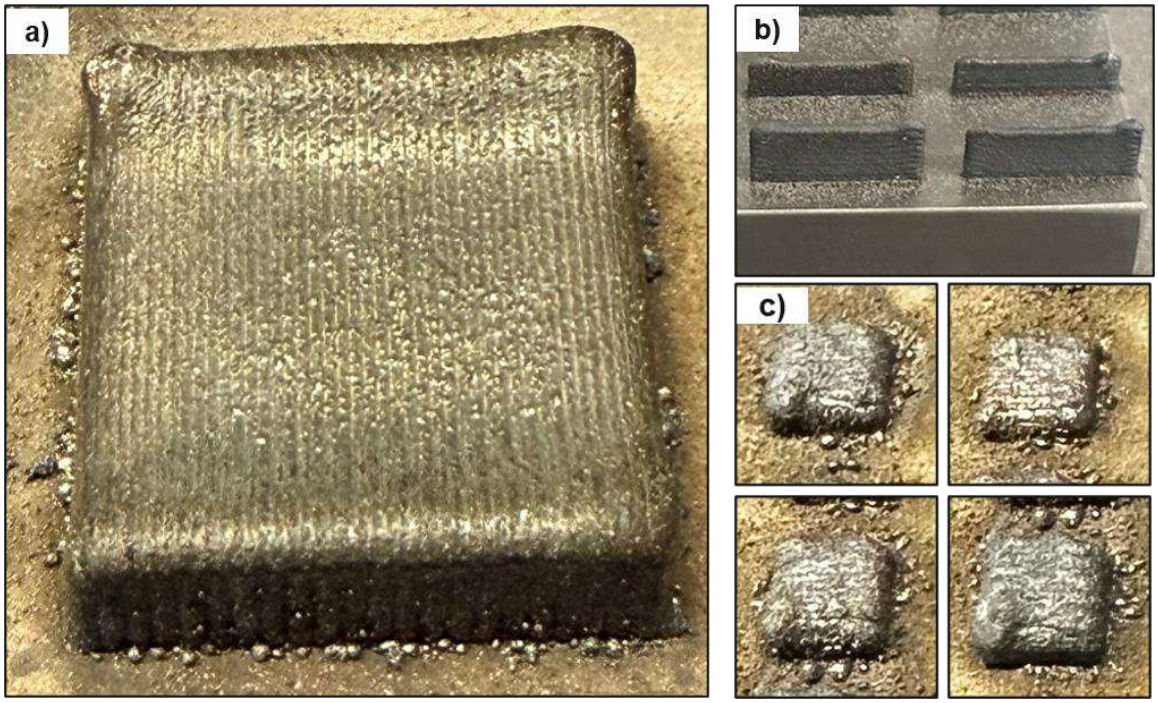


Fig. 7 *Printed SS316L samples: (a) 20 × 20 × 15 mm, 30-layer calibration block; (b) thin-wall validation prints, 20 mm long with 20 layers; (c) 5 × 5 × 2.5 mm, 5-layer validation cubes*

Meltpool width and length were extracted from the coaxial images of each layer, and the meltpool core temperature was taken from the hot spot of the infrared images. The printed cubes were scanned with the Keyence V700 series 3D scanner, and the part length, width, and height were measured from the scans.

6 Results and discussion

This section presents the calibration of the thermal-geometric model and its validation against the experiments described in Section 5. The model is first calibrated on the 30-layer block, and its predictions are then compared with the measured meltpool dimensions of the thin-walls and the measured part dimensions of the cubes.

The calibration sample was the 20 × 20 × 15 mm, 30-layer SS316L block described in Section 5 and shown in Fig. 7a. It was printed at a laser power of 350 W, a scan speed of 300 mm/min, and

a powder feed rate of 2 g/min, with a hatch spacing of 0.35 mm and a bidirectional scan pattern with no layer-to-layer rotation, together with a 0.5 mm beam spot diameter and 0.5 mm layer height. All process settings were held constant for the duration of the build. Only the first five layers were used for calibration, since the deposition was stable over these layers, whereas the later layers deviated from ideal deposition conditions.

The four model parameters ($\chi, r_{eff}, d_{eff}, \eta_0$) were calibrated using the meltpool core temperatures measured by the infrared camera in the first five layers of this build. The tuning was carried out by iterative trial and error: starting from approximate values, the model was run for multiple parameter combinations, and the parameters were adjusted iteratively until the predicted meltpool temperatures fell within the range of the measured temperatures.

After calibration, the predicted meltpool temperature and meltpool dimensions are presented in Fig. 8 and Fig. 9. Fig. 8 shows the predicted meltpool temperature over the first five layers. The temperature increases with successive layers, which is attributed to the accumulation of heat in the substrate from printing the previous layers. As the build progresses, the rising thermal baseline results in higher temperatures during subsequent deposition, demonstrating the layer-to-layer thermal inheritance captured by the model. The inset in Fig. 8 shows the meltpool temperature for Layer 1 only, where the temperature peaks repeatedly, once per track. This follows from the bidirectional scan pattern: at each turn, the laser starts the next track right beside the end of the previous one, which was deposited only a moment earlier and is still hot, so the meltpool temperature is momentarily highest there and then decreases as the laser moves away from this region.

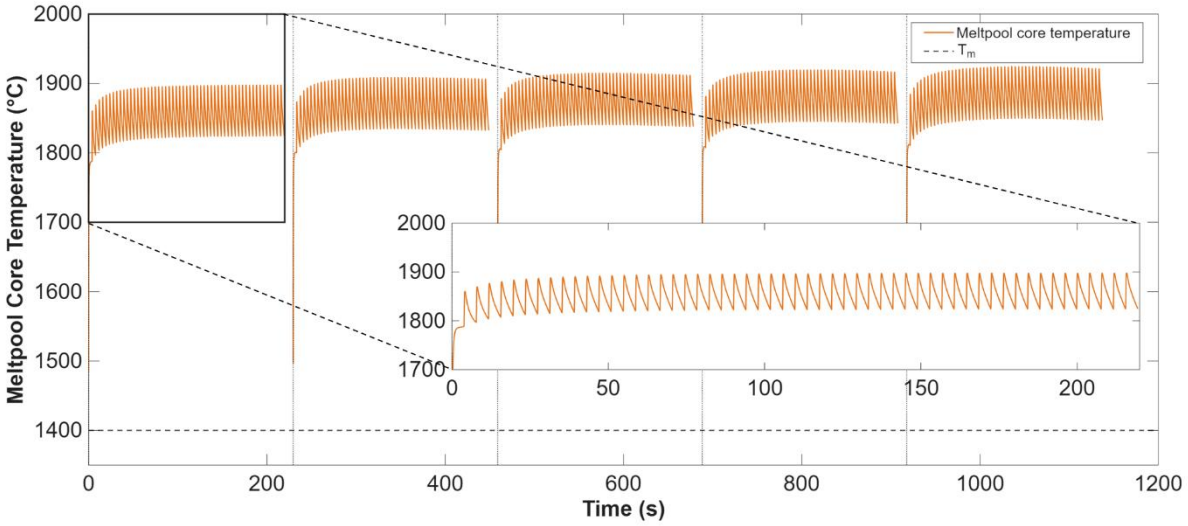


Fig. 8 *Simulated meltpool core temperature over the full five-layer build showing the temperature rise within each layer; the inset shows Layer 1, and track-to-track temperature elevation as the laser steps between tracks and the gradual rise in baseline temperature as the layer progresses*

A similar increasing trend is observed in the predicted meltpool dimensions, as shown in Fig. 9. Both the meltpool width and length increase with successive layers as a result of the increasing thermal accumulation within the part. The elevated substrate temperature reduces the amount of additional energy required to reach the melting temperature. As a result, more of the incoming laser energy is available for melting, which produces a larger and hotter meltpool. The larger meltpool intercepts and melts more powder, which increases the deposited volume per track and hence the predicted bead dimensions, so that the growth in meltpool size is reflected in the predicted deposition geometry.

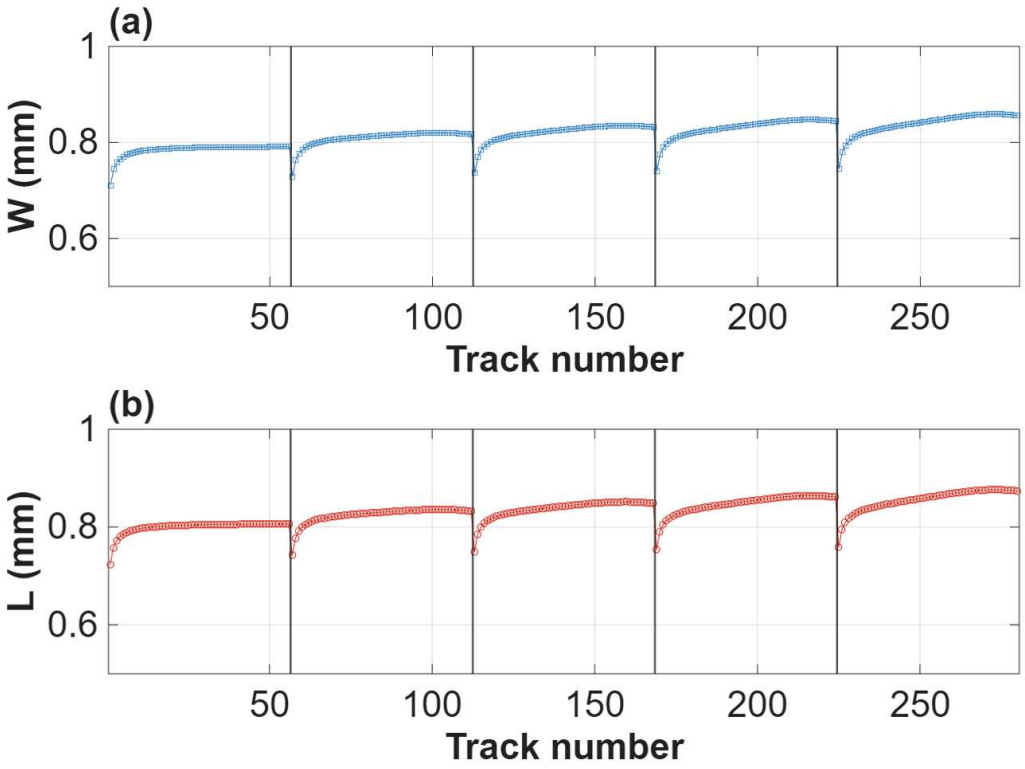
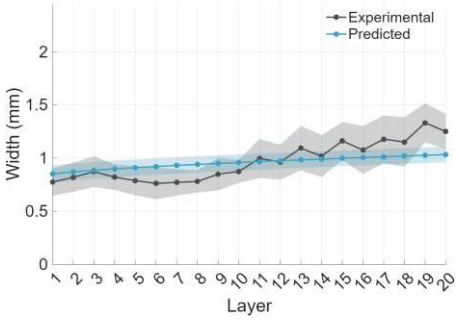
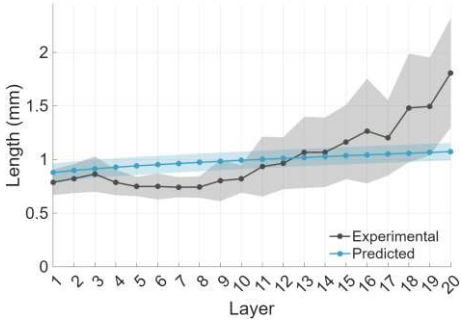
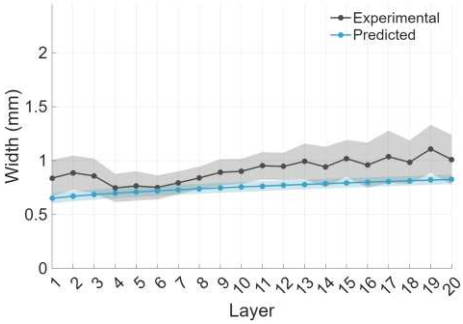
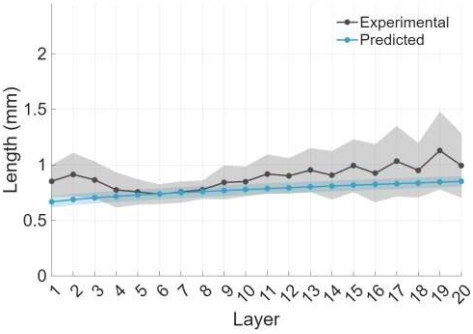


Fig. 9 *Simulated meltpool (a) width and (b) length for each track of the first five layers of the 30-layer calibration build (P = 350 W, v = 300 mm/min, F = 2 g/min). Vertical lines separate successive layers. Both dimensions increase within each layer and from layer to layer as heat accumulates in the part*

From the predicted meltpool width and bead height of each track, the three-dimensional profile of the deposited part is generated by accumulating the parabolic cross-sectional profiles of individual tracks across each layer, with the overlap between adjacent tracks accounted for through the continuity and mass-conservation conditions described in Section 4, and by stacking the resulting layer surfaces sequentially. The final build profile is therefore obtained from the predicted thermal history and track-level deposition geometry rather than being prescribed directly as an input. The predicted 3D profiles are compared with the 3D scans of the printed cubes in the validation below. The developed model was then validated on four independent thin-wall prints (Fig. 7b). The thin-walls were printed at a laser power of 400 W, with scan speeds of 400 and 600 mm/min and powder feed rates of 5.7 and 10.5 g/min, and with the print direction alternating from layer to layer. These conditions differ from those of the calibration build, so they test whether the model predicts meltpool dimensions beyond the calibration data. Fig. 10 compares the predicted and measured meltpool width and length for each layer of the four prints, and Table 2 lists the averages of meltpool dimensions for all layers. The predicted and measured values were closest for Print 1. For Prints 2 through 4, the predicted meltpool width and length were smaller than the measured

values, with the largest difference for Print 4, where both the scan speed and the powder feed rate were increased. The deviations thus increased as the scan speed and powder feed rate moved further from those of the calibration build. In the experimental data, the meltpool width and length decrease over the first few layers and then increase steadily for the remainder of the print, whereas the model predicts a gradual increase from the first layer. The steady increase after the initial layers is consistent with the rising baseline temperature predicted by the model, as heat accumulates in the wall. The initial decrease is not captured by the thermal model and is likely related to the initial deposition conditions rather than to the thermal history. The remaining deviations, in particular the under-prediction of the meltpool width and length for Prints 2–4, are partly due to experimental factors, such as variations in powder delivery and in the extraction of meltpool dimensions from the coaxial images.

Printed Parts	Meltpool Width	Meltpool Length
Print 1 		
Print 2 		

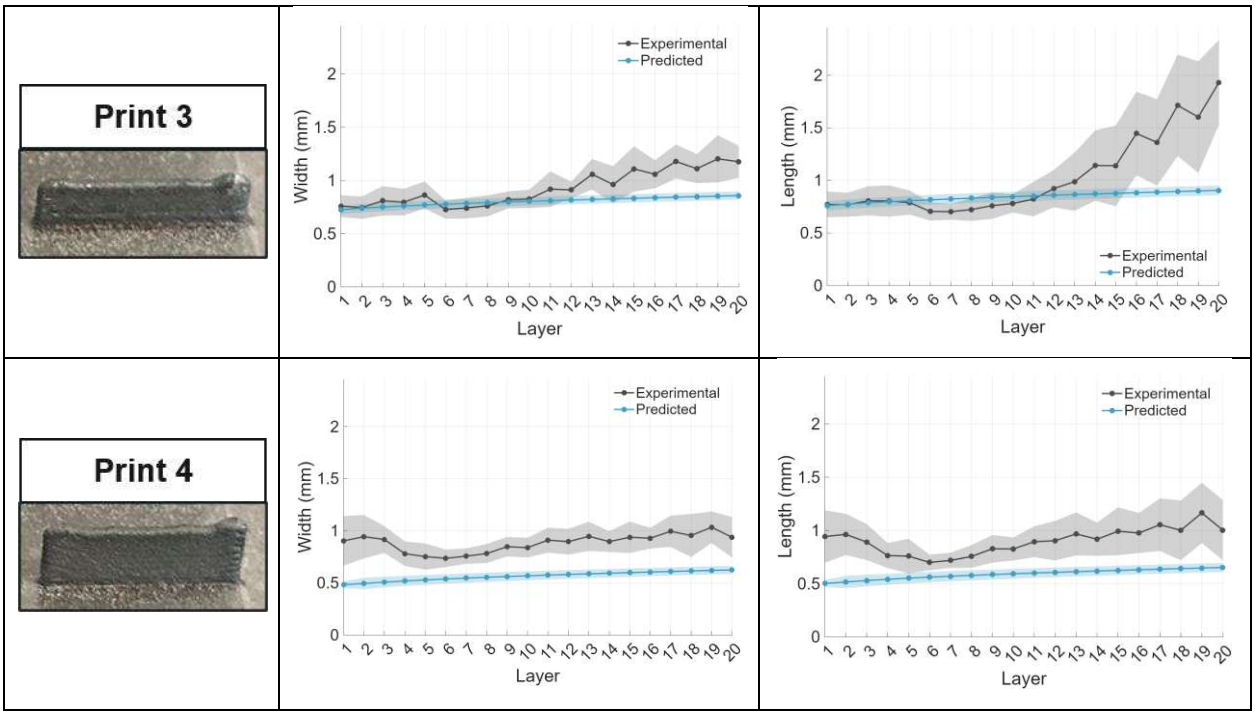


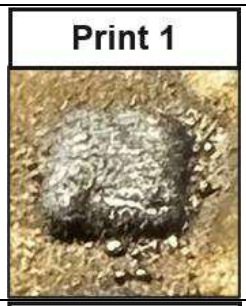
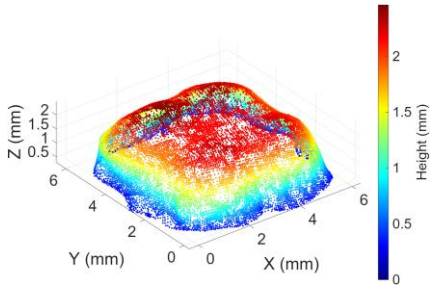
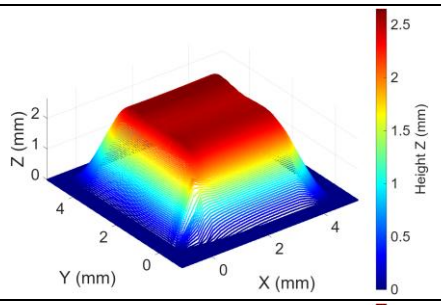
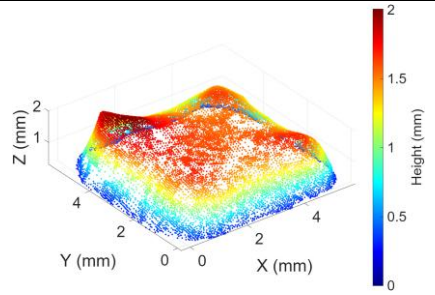
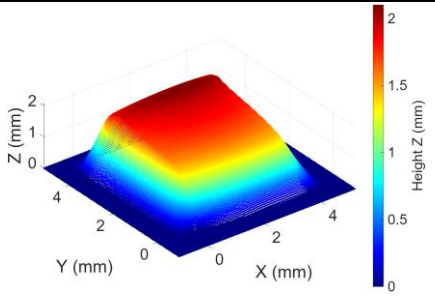
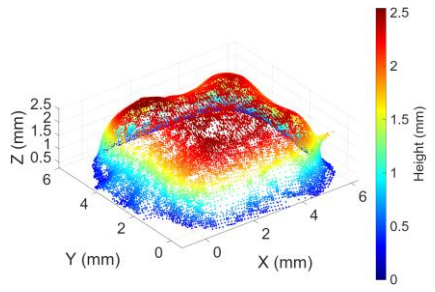
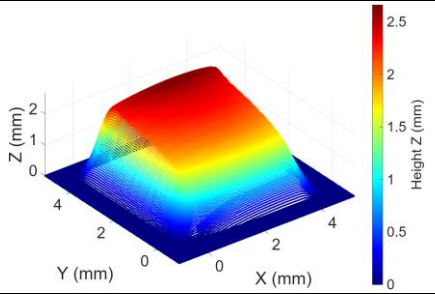
Fig. 10 *Thin-wall prints (left) and the experimental versus predicted meltpool width (middle) and length (right) for each layer of Prints 1–4; the shaded bands indicate ± one standard deviation about the mean of each layer*

Table 2 *Predicted and measured average meltpool width and length of the thin-wall prints*

Print No.	Laser Power (W)	Scan Speed (mm/min)	Powder feed rate (g/min)	Predicted Average (mm)		Measured Average (mm)		Model Deviation %	
				Meltpool Width	Meltpool Length	Meltpool Width	Meltpool Length	Meltpool Width	Meltpool Length
1	400	400	5.7	0.983	1.020	0.967	1.016	1.655	0.394
2	400	400	10.5	0.773	0.796	0.911	0.891	-15.148	-10.662
3	400	600	5.7	0.818	0.862	0.926	1.034	-11.663	-16.634
4	400	600	10.5	0.566	0.590	0.885	0.901	-36.045	-34.517
Average								16.128	15.552

The calibrated model was also validated on four 5 × 5 × 2.5 mm cube samples (Fig. 7c). Fig. 11 shows the printed cubes, their 3D scans, and the 3D profiles predicted by the model. The predicted length, width, and height were compared with the measured dimensions, and the results are listed in Table 3. The average absolute deviations were 13.72% for length, 8.55% for width, and 23.06% for height. These deviations correspond to mean absolute errors of 0.80, 0.49, and 0.60 mm, respectively. Consistent with the thin-wall results, the closest overall agreement was obtained for the cube printed with the calibration parameters (Print 1: 350 W, 300 mm/min, 2 g/min), with an average deviation of 9.5% across the three dimensions and a height deviation of only 7.57%, since

the four model parameters were calibrated from a single build at one set of process conditions. Across all four prints, which were simulated without re-calibration, the mean absolute errors remained below 1 mm. Fig. 11 also shows that the predicted 3D profiles capture the one-sided material buildup observed in the printed cubes at the end of each layer. Since the scan pattern was not rotated between layers, the last few tracks of every layer were deposited where the heat inherited from the preceding layers had accumulated (Fig. 3), creating a thermal gradient toward the end of the layer. The higher local temperature enlarged the meltpool, which captured more powder and deposited more material, and this effect compounded as the layers were stacked. This level of dimensional accuracy is sufficient for process planning, parameter screening, and the comparison of scan strategies, where identifying the better process conditions matters more than predicting exact dimensions.

Printed Parts	3D Scans	Predicted 3D profile
		
		
		

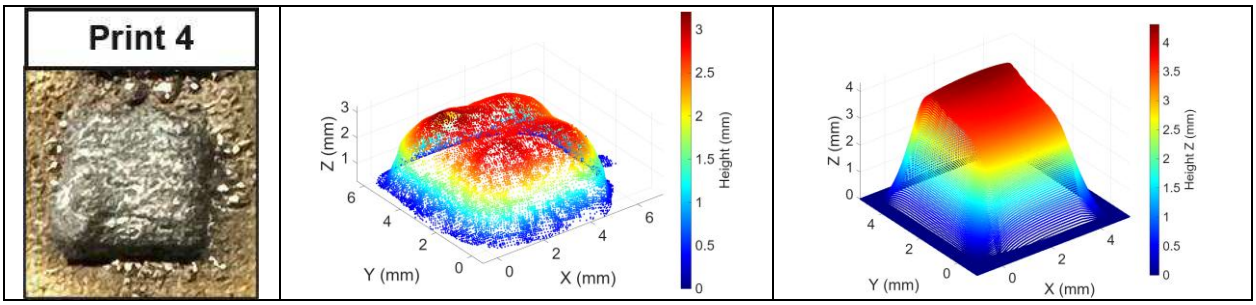


Fig. 11 *Printed 5 × 5 × 2.5 mm cube samples (left), their 3D scans (middle), and the 3D profiles predicted by the model (right) for Prints 1–4*

Table 3 *Predicted and measured length, width, and height of the cube samples, with the model deviation for each dimension*

Print No.	Power (W)	Scan Speed (mm/min)	Feed rate (g/min)	Measured Dimensions (mm)			Predicted Dimensions (mm)			Model Deviation %		
				L	W	H	L	W	H	L	W	H
1	350	300	2	5.95	5.85	2.46	5.19	5.38	2.65	-12.80	-8.03	7.57
2	300	300	2	5.48	5.47	2.00	4.84	5.03	2.66	-11.66	-8.13	32.77
3	300	300	2.9	5.94	5.69	2.54	5.15	5.09	2.10	-13.24	-10.64	-17.42
4	350	300	2.9	5.90	5.79	3.21	4.88	5.36	4.31	-17.23	-7.40	34.49
Mean Absolute Model Deviation										13.72	8.55	23.06

Overall, the model predicted the meltpool dimensions and the 3D profile of the printed parts with reasonable agreement, with average deviations between 8.6% and 23.1% across all predicted dimensions, for different print geometries and scan patterns, while also capturing the direction-dependent heat accumulation that results from an unrotated scan pattern. The computation time of the model was 1416.5 s for the 30-layer block, 268.6 s for a thin-wall, and 454.5 s for a cube. The main findings of this study are summarized as follows.

For the thin-walls, the predicted meltpool width and length deviated from the measurements by 16.1% and 15.6% on average, with the closest agreement, within 2%, obtained for the print with the lowest scan speed and powder feed rate (Print 1). At higher feed rates and scan speeds, the predicted meltpool was consistently smaller than the measured one. The comparison in Table 2 shows that the model reproduced the measured trends, a smaller meltpool at higher powder feed rate and scan speed, but responded to these changes more strongly than the process: between Print 1 and Print 4, the predicted meltpool width and length decreased by about 42%, whereas the measured values decreased by only 8% and 11%. This higher sensitivity follows from the energy balance on which the model is built, in which the meltpool size is set by the net energy delivered per unit length of track, and reflects three simplifications adopted to retain a closed-form,

computationally efficient formulation. First, the laser energy attenuated by the powder cloud is treated as entirely removed from the system (Eqs. (12)–(13), Section 3.5). This represents the largest possible energy loss and hence the smallest energy available for melting, whereas in practice part of this energy is absorbed by particles that subsequently enter the meltpool, so that the net energy loss increases more slowly with powder feed rate than assumed [26]. Second, the semi-infinite substrate, adopted to obtain a closed-form solution, allows heat to be conducted away in all directions, whereas a thin-wall can conduct heat only through its base; the shorter layer times at higher scan speed therefore lead to greater heat accumulation in the wall, which partly offsets the lower energy input per unit length. Third, in the process, the meltpool width is constrained by the laser spot and powder stream size, which were identical for all prints, whereas in the model it is determined by the extent of the melting isotherm (Section 4). As a result, the model under-predicts the meltpool dimensions, i.e., the predicted meltpool dimensions are close to or smaller than the measured ones, so that a track overlap predicted to be sufficient by the model is also achieved in the process. In addition, the model amplifies the differences between process conditions, which is advantageous when comparing candidate parameter sets.

For the cubes, the predicted length, width, and height deviated from the measurements by 13.72%, 8.55%, and 23.06% on average, corresponding to mean absolute errors of 0.80, 0.49, and 0.60 mm. The length and width were under-predicted by a similar margin for all four cubes, independent of laser power and powder feed rate and including the cube printed with the calibration parameters, which indicates a systematic offset, i.e., a deviation of consistent sign and similar magnitude for all process conditions, rather than a deviation that changes with the process parameters. Since the offset was of similar magnitude for all four cubes, including Print 1, which was printed with the same process parameters as the calibration build, it is attributed to the definition of the part edges rather than to the predicted thermal field. In the model, the lateral extent of the part is defined by the meltpool boundary of the outermost tracks (Section 4), whereas the 3D scans capture the outer surface of the deposit, which extends beyond this boundary because the molten material of the outermost tracks, which are supported on one side only, spreads over the edges of the underlying layers, and partially melted powder particles from the periphery of the powder stream adhere to the side walls. The additional deposition at the track ends, where the laser turns around between successive tracks, further accounts for the larger offset along the scan direction. The height deviated in both directions because, in the model, the bead height depends on the meltpool width

through two competing effects: a wider meltpool captures a larger fraction of the powder stream (Eq. (22)), which increases the deposited area (Eq. (23)), but distributes this area over a wider bead (Eq. (24)), which reduces its height. Depending on the process conditions, either effect can dominate, so that the height deviations do not follow a consistent trend; nevertheless, the mean absolute height error of 0.60 mm corresponds to approximately one layer height (0.5 mm) over the five-layer build. The predicted 3D profiles also reproduced the one-sided material buildup caused by the unrotated scan pattern.

These results show that the heat accumulated from previous layers governs the growth of the meltpool and the material buildup at the end of each layer, and that a single calibration build is sufficient for the model to predict these trends for different geometries and process conditions. With simulation times of 4.5–24 min per build, the model can therefore be used to screen process parameters and compare scan strategies before printing, reducing the number of trial-and-error builds.

7 Conclusion

This study developed an analytical thermal model for multi-layer, multi-track laser powder directed energy deposition (LP-DED) of SS316L and coupled it with a parabolic cross-section geometry model to predict meltpool dimensions and the 3D print profile directly from the process parameters and toolpath. The thermal model extends the classical Gaussian moving-source solution with three mechanisms that become significant over the timescale of a multi-layer build: lumped surface heat loss, the enthalpy sink of powder entering the meltpool, and attenuation of the beam by the powder cloud. Its principal extension is the treatment of layer-to-layer thermal inheritance as a spatially resolved carry-over field rather than a single averaged substrate temperature, which captures the measurable difference in preheat between the start and end of a layer's toolpath.

The two models are solved in sequence: the thermal model yields the meltpool width from the predicted isotherm, and the geometry model uses this width together with a powder catchment mass balance to obtain the bead height. With its four parameters calibrated from a single build using infrared-measured meltpool core temperatures, the model predicted the meltpool width and

length of the thin-walls with average deviations of 16.1% and 15.6%, and within 2% at the lowest scan speed and powder feed rate, and the length, width, and height of the cubes with mean absolute errors of 0.80, 0.49, and 0.60 mm. Since the laser energy attenuated by the powder stream is treated as entirely lost, an upper bound on this energy loss, the model under-predicts the meltpool dimensions, i.e., the predicted meltpool dimensions are close to or smaller than the measured ones, at powder feed rates above that of the calibration build, and its prediction accuracy can be further improved by calibration within the nominal processing window of the intended application. It also reproduced the one-sided material buildup that arises when the scan pattern is not rotated between layers, and simulated each build within 4.5–24 min, which makes it suitable for rapid process planning and parameter selection.

The proposed thermal-geometry model provides a fast, physics-based means of predicting the outcome of multi-layer, multi-track LP-DED builds. Unlike single-track and single-layer analytical models, it accounts for layer-to-layer heat accumulation and the path dependence of the temperature field, and it links this thermal history directly to the deposited geometry. Once its four effective parameters have been calibrated from a single build for the system and material considered, the model requires only the process parameters, toolpath, and part geometry as inputs and simulates a complete build within minutes, whereas finite-element models are computationally demanding for multi-layer builds [3, 10]. These characteristics make it possible to screen process parameters, compare scan strategies, and interpret in-situ meltpool measurements before material and machine time are committed, thereby reducing the reliance on trial-and-error builds, and they make the model a suitable basis for digital twins and data-driven process models.

The short computation time also makes the model a practical source of synthetic data for training data-driven models. Experimental LP-DED data are costly to acquire, because each build requires substrate preparation, powder loading, and machine setup, followed by the deposition itself, cooling of the part, and post-build characterization such as 3D scanning and image processing. Each build also consumes powder, of which only a fraction is incorporated into the part, together with substrate material and shielding gas. In addition, the process space defined by laser power, scan speed, powder feed rate, hatch spacing, and scan strategy is large: sampling only four levels of each of these five parameters would already require $4^5 = 1024$ experimental builds, each involving the preparation, deposition, and measurement steps described above. The present model,

in contrast, simulates a thin-wall in under 5 min and a cube in under 8 min without consuming any material or machine time, and since the simulations of different parameter combinations are independent of one another, they can be distributed across multiple computers to generate large datasets rapidly. Each simulation yields a labeled data point that links the input process parameters to the resulting temperature history, meltpool dimensions, and part geometry, and such datasets can be used to train machine-learning surrogate models for real-time monitoring and closed-loop control of LP-DED.

Future work will apply the model to complex geometries with complex print patterns and toolpaths, beyond the blocks, thin-walls, and cubes studied here. Since the model computes the temperature field and the deposited geometry directly from the toolpath and the process parameters, it can be used to compare scan strategies, such as rotated or island patterns, before printing, and to reduce effects such as the one-sided material buildup observed in this study. Extending the geometry model to curved and varying-height surfaces would be required for such parts. In addition, calibrating the model against builds that span a wider range of process conditions is expected to extend the range over which it accurately predicts meltpool and part dimensions.

References

1. Saboori A, Aversa A, Marchese G, Biamino S, Lombardi M, Fino P (2019) Application of directed energy deposition-based additive manufacturing in repair. Appl Sci 9:3316. https://doi.org/10.3390/app9163316

2. Dass A, Moridi A (2019) State of the art in directed energy deposition: from additive manufacturing to materials design. Coatings 9:418. https://doi.org/10.3390/coatings9070418

3. DebRoy T, Wei HL, Zuback JS, Mukherjee T, Elmer JW, Milewski JO, Beese AM, Wilson-Heid A, De A, Zhang W (2018) Additive manufacturing of metallic components – process, structure and properties. Prog Mater Sci 92:112–224. https://doi.org/10.1016/j.pmatsci.2017.10.001

4. Everton SK, Hirsch M, Stravroulakis P, Leach RK, Clare AT (2016) Review of in-situ process monitoring and in-situ metrology for metal additive manufacturing. Mater Des 95:431–445. https://doi.org/10.1016/j.matdes.2016.01.099

5. Errico V, Campanelli SL, Angelastro A, Dassisti M, Mazzarisi M, Bonserio C (2021) Coaxial monitoring of AISI 316L thin walls fabricated by direct metal laser deposition. Materials 14:673. https://doi.org/10.3390/ma14030673

6. Tang L, Landers RG (2010) Melt pool temperature control for laser metal deposition processes—Part I: online temperature control. J Manuf Sci Eng 132:011010. https://doi.org/10.1115/1.4000882

7. Tang L, Landers RG (2010) Melt pool temperature control for laser metal deposition processes—Part II: layer-to-layer temperature control. J Manuf Sci Eng 132:011011. https://doi.org/10.1115/1.4000883

8. Heigel JC, Michaleris P, Reutzel EW (2015) Thermo-mechanical model development and validation of directed energy deposition additive manufacturing of Ti–6Al–4V. Addit Manuf 5:9–19. https://doi.org/10.1016/j.addma.2014.10.003

9. Wang L, Felicelli S (2006) Analysis of thermal phenomena in LENS™ deposition. Mater Sci Eng A 435–436:625–631. https://doi.org/10.1016/j.msea.2006.07.087

10. Fetni S, Maurizi Enrici T, Niccolini T, Tran HS, Dedry O, Duchêne L, Mertens A, Habraken AM (2021) Thermal model for the directed energy deposition of composite coatings of 316L stainless steel enriched with tungsten carbides. Mater Des 204:109661. https://doi.org/10.1016/j.matdes.2021.109661

11. Rosenthal D (1946) The theory of moving sources of heat and its application to metal treatments. Trans ASME 68:849–866

12. Eagar TW, Tsai NS (1983) Temperature fields produced by traveling distributed heat sources. Weld J 62(12):346s–355s

13. Goldak J, Chakravarti A, Bibby M (1984) A new finite element model for welding heat sources. Metall Trans B 15:299–305. https://doi.org/10.1007/BF02667333

14. Nguyen NT, Ohta A, Matsuoka K, Suzuki N, Maeda Y (1999) Analytical solutions for transient temperature of semi-infinite body subjected to 3-D moving heat sources. Weld J 78(8):265s–274s

15. Carslaw HS, Jaeger JC (1959) Conduction of heat in solids, 2nd edn. Oxford University Press, Oxford

16. Hu D, Kovacevic R (2003) Modelling and measuring the thermal behaviour of the molten pool in closed-loop controlled laser-based additive manufacturing. Proc Inst Mech Eng B J Eng Manuf 217:441–452. https://doi.org/10.1243/095440503321628125

17. Ansari M, Martinez-Marchese A, Huang Y, Toyserkani E (2020) A mathematical model of laser directed energy deposition for process mapping and geometry prediction of Ti-5553 single-tracks. Materialia 12:100710. https://doi.org/10.1016/j.mtla.2020.100710

18. Ansari M, Martinez-Marchese A, Khamooshi M, Keshavarzkermani A, Esmaeilizadeh R, Toyserkani E (2022) Analytical modeling of multi-track powder-fed laser directed energy deposition: on the relationships among process, deposition dimensions, and solidification microstructure in additively manufactured near-β titanium alloy. J Mater Process Technol 306:117643. https://doi.org/10.1016/j.jmatprotec.2022.117643

19. Mirkoohi E, Ning J, Bocchini P, Fergani O, Chiang K-N, Liang SY (2018) Thermal modeling of temperature distribution in metal additive manufacturing considering effects of build layers, latent heat, and temperature-sensitivity of material properties. J Manuf Mater Process 2:63. https://doi.org/10.3390/jmmp2030063

20. Huang Y, Khamesee MB, Toyserkani E (2019) A new physics-based model for laser directed energy deposition (powder-fed additive manufacturing): from single-track to multi-track and multi-layer. Opt Laser Technol 109:584–599. https://doi.org/10.1016/j.optlastec.2018.08.015

21. Pinkerton AJ, Li L (2004) Modelling the geometry of a moving laser melt pool and deposition track via energy and mass balances. J Phys D Appl Phys 37:1885–1895. https://doi.org/10.1088/0022-3727/37/14/003

22. Sobhanieh N, Akbari J, Moradi M (2022) A new method for calculating laser intensity distribution on workpiece surface in laser-directed energy deposition process by considering powder stream distribution and laser attenuation. Int J Adv Manuf Technol 121:337–348. https://doi.org/10.1007/s00170-022-09301-1

23. Ocelík V, Nenadl O, Palavra A, De Hosson JThM (2014) On the geometry of coating layers formed by overlap. Surf Coat Technol 242:54–61. https://doi.org/10.1016/j.surfcoat.2014.01.018

24. Nenadl O, Kuipers W, Koelewijn N, Ocelík V, De Hosson JThM (2016) A versatile model for the prediction of complex geometry in 3D direct laser deposition. Surf Coat Technol 307:292–300. https://doi.org/10.1016/j.surfcoat.2016.08.090

25. Gockel J, Klingbeil N, Bontha S (2016) A closed-form solution for the effect of free edges on melt pool geometry and solidification microstructure in additive manufacturing of thin-wall geometries. Metall Mater Trans B 47:1400–1408. https://doi.org/10.1007/s11663-015-0547-z

26. Frenk A, Vandyoussefi M, Wagnière JD, Zryd A, Kurz W (1997) Analysis of the laser-cladding process for stellite on steel. Metall Mater Trans B 28:501–508. https://doi.org/10.1007/s11663-997-0117-0

Statements and Declarations

Funding: This research did not receive any specific grant from external funding.

Competing interests: The authors have no relevant financial or non-financial interests to disclose.

Author contributions: Sudharshanan Dhabaseelan Vasugi: Conceptualization, Methodology, Software, Investigation, Formal analysis, Data curation, Visualization, Writing – original draft. Chaitanya Krishna Prasad Vallabh: Conceptualization, Resources, Supervision, Writing – review and editing. Souran Manoochehri: Conceptualization, Supervision, Writing – review and editing. All authors read and approved the final manuscript.

Acknowledgments: The authors thank Dr. Youmna Mahmoud (Stevens Institute of Technology) for acquiring the meltpool data for the thin-wall prints used in model validation in this study.